Journal of Computational Physics 228 (2009) 5129–5147

Contents lists available at ScienceDirect

Journal of Computational Physics

journal homepage: www.elsevier.com/locate/jcp

Multiscale finite-volume method for parabolic problems arising from compressible multiphase flow in porous media

Hadi Hajibeygi *, Patrick Jenny

Institute of Fluid Dynamics, ETH Zurich, Sonneggstrasse 3, Zurich CH-8092, Switzerland

A R T I C L E I N F O

Article history:
Received 7 November 2008
Received in revised form 30 March 2009
Accepted 6 April 2009
Available online 22 April 2009

Keywords:
Multiscale method
Multiscale finite-volume method
Compressible flow
Multiphase flow
Parabolic problems
Porous media
Iterative multiscale methods
Iterative multiscale finite-volume method
Reservoir simulation

A B S T R A C T

The multiscale finite-volume (MSFV) method was originally developed for the solution of heterogeneous elliptic problems with reduced computational cost. Recently, some extensions of this method for parabolic problems have been proposed. These extensions proved effective for many cases, however, they are neither general nor completely satisfactory. For instance, they are not suitable for correctly capturing the transient behavior described by the parabolic pressure equation. In this paper, we present a general multiscale finite-volume method for parabolic problems arising, for example, from compressible multiphase flow in porous media. Opposed to previous methods, here, the basis and correction functions are solutions of full parabolic governing equations in localized domains. At the same time, to enhance the computational efficiency of the scheme, the basis functions are kept pressure independent and do not have to be recalculated as pressure evolves. This general approach requires no additional assumptions and its good efficiency and high accuracy is demonstrated for various challenging test cases. Finally, to improve the quality of the results and also to extend the scheme for highly anisotropic heterogeneous problems, it is combined with the iterative MSFV (i-MSFV) method for parabolic problems. As one iterates, the i-MSFV solutions of compressible multiphase problems (parabolic problems) converge to the corresponding fine-scale reference solutions in the same way as demonstrated recently for incompressible cases (elliptic problems). Therefore, the proposed MSFV method can also be regarded as an efficient linear solver for parabolic problems and studies of its efficiency are presented for many test cases.

1. Introduction

Current advances in characterization and data integration for natural porous media provide increasingly detailed descriptions of the formations, which are essential for accurate reservoir simulations. Unfortunately, classical simulation techniques are too expensive at this level of resolution. Therefore, various multiscale methods have been developed during the past decade [1–12] based on the fact that solving many local problems is more efficient than solving one global system. Hence, localized problems are considered and sets of numerically computed basis functions (honoring the provided permeability field) are employed to solve the problem on a coarse grid. The approximate fine-scale solution is reconstructed based on the coarse-scale solution. It has been demonstrated for a wide range of test cases that this solution field is in good agreement with the results obtained by solving the global fine-scale system. Among the proposed multiscale methods, Mixed Multiscale Finite Element (MMSFE) methods [6,9,11,13] and the multiscale finite-volume (MSFV) method [7,14–16] provide locally conservative velocity fields, which is crucial for accurately solving the saturation transport equations.

* Corresponding author. Tel.: +41 44 632 6034; fax: +41 44 632 1147.
E-mail addresses: hajibeygi@ifd.mavt.ethz.ch (H. Hajibeygi), jenny@ifd.mavt.ethz.ch (P. Jenny).

0021-9991/$ - see front matter © 2009 Elsevier Inc. All rights reserved.
doi:10.1016/j.jcp.2009.04.017

The MSFV method was proposed by Jenny et al. [7,14–16] for heterogeneous elliptic problems arising from incompressible multiphase flow in porous media. Later, to capture the fine-scale source terms and also capillary and gravitational effects accurately, another set of functions with local support (correction functions) were introduced by Lunati and Jenny [17,18]. Correction functions are particular (non-scalable) numerical solutions of the problem in the localized small domains. The MSFV method has also been extended to incorporate complex wells [19–21]. Recently, to improve the quality and the application of the MSFV method for extremely heterogeneous anisotropic problems, the iterative MSFV (i-MSFV) method to converge multiscale solutions to the corresponding fine-scale reference solutions was developed by Hajibeygi et al. [22]. The idea of the i-MSFV method is based on improving the localization condition iteratively using the smoothed approximate MSFV solution. It is also important that the conservative solution field can be reconstructed after any iteration step. Therefore, the i-MSFV method can be used anywhere between a pure multiscale and an efficient linear solver. More recently, Bonfigli and Jenny used the i-MSFV method as an efficient Poisson solver for the incompressible Navier–Stokes equations with immersed boundaries [23].

The MSFV method was also extended for the solution of parabolic problems arising from compressible multiphase flow in porous media through three major works [24–26]. The proposed approaches proved to be effective for many cases, however, there still exists potential for significant improvement.

Lunati and Jenny [24] neglected compressibility effects inside the localized domains in order to avoid a frequent update of the basis functions. In their approach, only the coarse-scale system accounts for the compressibility effects. This scheme is computationally efficient, but requires additional assumptions. Later, Zhou and Tchelepi [25] relaxed this assumption only in the elliptic part of the localized problems. In their Operator Based Multiscale Method (OBMM), accumulation terms only appear in the coarse-scale system. In some of the difficult cases, the results of this approach are in better agreement with the corresponding fine-scale solutions. However, also the OBMM cannot properly capture the transient fine-scale behavior. None of the above-mentioned approaches involves correction functions. Recently, Lee et al. [26] employed correction functions to account for the accumulation terms in the localized domains. In their work, similar to [25], basis functions are still numerical solutions of the elliptic part of the full parabolic problem and must be recomputed in each iteration step. Despite updating the basis functions adaptively helps to improve the computational efficiency of the scheme, it is favorable to keep the basis functions pressure level independent.

In this paper, first a general MSFV framework for parabolic problems is presented. In the new method, the basis functions are kept independent of the pressure field. Such an approach is not only more general and accurate than previous methods; at the same time it is also efficient. Moreover, to construct the coarse system, exactly the same procedure applies as for the incompressible (elliptic) MSFV method.

In a second part, the i-MSFV method for compressible multiphase flow in porous media (parabolic problems) is presented. Similar to the i-MSFV method for elliptic problems [22], the solution field is smoothed in each iteration step and used to improve the localization condition for the next iteration step. So far, only a limited set of smoothers has been explored. For highly anisotropic heterogeneous problems (or for simulations with a stretched grid), however, line-relaxation proved to be very effective [22] and hence was used as a smoother for this work.

The paper is organized as follows. In Section 2, the governing equations and the fine-scale discretization are presented. The standard MSFV method for elliptic problems is explained in Section 3. Based on that, in Section 4 the new MSFV method for parabolic problems arising from compressible multiphase flow in porous media is introduced. Numerical test cases are presented in Section 5 and in Section 6, the i-MSFV method for compressible multiphase flow is introduced. In Section 7, its numerical convergence is studied for different test cases and finally the paper is concluded.

2. Governing equations and fine-scale discretization

For simplicity, but without loss of generality, no dissolution and no capillary effects are considered here. In this case, Darcy's formulation of multiphase flow in porous media leads to the mass conservation law

$$\frac{\partial}{\partial t}(\phi\rho_\alpha S_\alpha) - \nabla\cdot(\rho_\alpha \boldsymbol{\lambda}_\alpha\cdot(\nabla p - \rho_\alpha g\nabla z)) = \rho_\alpha q_\alpha \quad \forall\alpha\in\{1,\ldots,\gamma\} \tag{1}$$

of phase α, where ϕ denotes the porosity, ρ_α the density, S_α the saturation, g the gravitational acceleration, and q_α source terms. Moreover, $\boldsymbol{\lambda}_\alpha = \boldsymbol{K}k_{r\alpha}/\mu_\alpha$ is the phase mobility with the positive definite permeability tensor $\boldsymbol{K}$, the relative permeability $k_{r\alpha}$, and the phase viscosity μ_α. Porosity, density and viscosity are given as algebraic functions of the pressure p and $k_{r\alpha}$ is a function of the saturations. Phase saturations are subject to the constraint

$$\sum_{\alpha=1}^{\gamma} S_\alpha = 1. \tag{2}$$

Note that Eqs. (1) and (2) form a system for $\gamma + 1$ unknowns $(S_1,\ldots,S_\alpha,p)$ [27].

Implicit Euler time integration leads to

$$\frac{\phi^{n+1}\rho_\alpha^{n+1}S_\alpha^{n+1} - \phi^n\rho_\alpha^n S_\alpha^n}{\Delta t} - \nabla\cdot\left(\rho_\alpha^{n+1}\boldsymbol{\lambda}_\alpha\cdot\left(\nabla p^{n+1} - \rho_\alpha^{n+1} g\nabla z\right)\right) = \rho_\alpha^{n+1}q_\alpha, \tag{3}$$

which is now divided by the density ρ_α^{n+1} in order to obtain a decoupled pressure equation. This is achieved by then taking the sum over all phases α resulting in

$$\frac{\phi^{n+1}}{\Delta t} - \frac{\phi^n}{\Delta t}\sum_{\alpha=1}^{\gamma} B_\alpha^{n+1}\rho_\alpha^n S_\alpha^n - \sum_{\alpha=1}^{\gamma} B_\alpha^{n+1}\nabla\cdot\left(\rho_\alpha^{n+1}\boldsymbol{\lambda}_\alpha\cdot\left(\nabla p^{n+1} - \rho_\alpha^{n+1} g\nabla z\right)\right) = q, \tag{4}$$

where $q = \sum_{\alpha=1}^{\gamma} q_\alpha$ denotes the total volumetric source term and $B_\alpha = 1/\rho_\alpha$ is the volume formation factor. Linearization of this equation results in the iterative linear pressure equation

$$\frac{C}{\Delta t}(p^{\nu+1} - p^\nu) - \sum_{\alpha=1}^{\gamma} B_\alpha^\nu \nabla\cdot(\rho_\alpha^\nu\boldsymbol{\lambda}_\alpha\cdot\nabla p^{\nu+1}) = -\frac{\phi^\nu}{\Delta t} + \frac{\phi^n}{\Delta t}\sum_{\alpha=1}^{\gamma} B_\alpha^\nu\rho_\alpha^n S_\alpha^n + q - \sum_{\alpha=1}^{\gamma} B_\alpha^\nu\nabla\cdot(\rho_\alpha^{\nu 2}\boldsymbol{\lambda}_\alpha g\cdot\nabla z), \tag{5}$$

which converges to Eq. (4) as $\nu \to \infty$. The superscripts ν and $\nu + 1$ denote quantities at the old and new iteration levels, respectively, and

$$C = \left.\frac{\partial\phi}{\partial p}\right|^\nu - \phi^n\sum_{\alpha=1}^{\gamma}\left.\frac{\partial B_\alpha}{\partial p}\right|^\nu \rho_\alpha^n S_\alpha^n \tag{6}$$

is the compressibility coefficient. Note that the coefficients B_α and ρ_α in the convective and gravitational terms lag one iteration behind. This discretized formulation was already used in previous studies to solve the fine-scale problem [25,26].

Here, however, for the sake of a more efficient MSFV formulation, which will be explained later, the convective term is consistently modified as

$$\sum_{\alpha=1}^{\gamma} B_\alpha^\nu\nabla\cdot(\rho_\alpha^\nu\boldsymbol{\lambda}_\alpha\cdot\nabla p^{\nu+1}) \approx \nabla\cdot(\boldsymbol{\lambda}_t\cdot\nabla p^{\nu+1}) - \nabla\cdot(\boldsymbol{\lambda}_t\cdot\nabla p^\nu) + \sum_{\alpha=1}^{\gamma} B_\alpha^\nu\nabla\cdot(\rho_\alpha^\nu\boldsymbol{\lambda}_\alpha\cdot\nabla p^\nu), \tag{7}$$

where $\boldsymbol{\lambda}_t = \sum_{\alpha=1}^{\gamma}\boldsymbol{\lambda}_\alpha$ is the total mobility. Note that $\nu = \nu + 1 = n + 1$, if converged. It is worth mentioning that for black-oil models, which are more realistic to describe multiphase flow in oil reservoirs [27], one can still use this expression. Additional effects are, e.g. capillary pressure differences and mass exchange between phases, which are treated on the right-hand side, i.e. the implicit convection operator has the same structure as in Eq. (7) [26]. Finally, our convergent iterative scheme for the fine-scale pressure equation reads

$$\frac{C}{\Delta t}(p^{\nu+1} - p^\nu) - \nabla\cdot(\boldsymbol{\lambda}_t\cdot\nabla p^{\nu+1}) = RHS^\nu, \tag{8}$$

where

$$RHS^\nu = -\frac{\phi^\nu}{\Delta t} + \frac{\phi^n}{\Delta t}\sum_{\alpha} B_\alpha^\nu\rho_\alpha^n S_\alpha^n - \sum_{\alpha=1}^{\gamma} B_\alpha^\nu\nabla\cdot(\rho_\alpha^{\nu 2}\boldsymbol{\lambda}_\alpha g\cdot\nabla z) + q - \nabla\cdot(\boldsymbol{\lambda}_t\cdot\nabla p^\nu) + \sum_{\alpha}^{\gamma} B_\alpha^\nu\nabla\cdot\left(\rho_\alpha^\nu\boldsymbol{\lambda}_\alpha\cdot\nabla p^\nu\right). \tag{9}$$

Here, $\boldsymbol{\lambda}_\alpha$ is calculated based on S_α^n leading to an IMPES (Implicit in Pressure, Explicit in Saturation) scheme. In other words, Eq. (8) is solved until convergence occurs, then the new pressure field is used to solve the saturation Eq. (3) explicitly using a second order upwind scheme. Note that alternatively, Eq. (3) can be solved implicitly, thus leading to a sequentially implicit scheme [24–26]. It is an important property for relation (8) that except of the accumulation term its structure is the same as for elliptic problems. Next, we will explain how one can solve an elliptic (incompressible) or parabolic (compressible) pressure equation using the MSFV method.

3. MSFV method for incompressible multiphase flow (elliptic)

First, before the new MSFV method for compressible problems will be explained, the previously developed MSFV method is described here. Therefore, we consider the elliptic problem

$$-\nabla\cdot(\boldsymbol{\lambda}_t\cdot\nabla p) = q \tag{10}$$

on the domain Ω with the boundary conditions $\nabla p\cdot\boldsymbol{n} = \zeta$ and $p = \xi$ at $\partial\Omega_1$ and $\partial\Omega_2$, respectively. Note that $\partial\Omega = \partial\Omega_1 \cup \partial\Omega_2$ with $\partial\Omega_1 \cap \partial\Omega_2 = \emptyset$ is the whole boundary of the domain Ω and $\boldsymbol{n}$ is the unit normal vector pointing outwards. The mobility tensor $\boldsymbol{\lambda}_t$ is positive definite and the right-hand sides q, ζ, and ξ are specified fields.

The MSFV method relies on an imposed coarse grid (solid lines in Fig. 1) and on a dual coarse grid (dashed lines in Fig. 1). The former is composed of M control volumes $\bar{\Omega}_k$ ($k \in [1,M]$) and the latter of N cells $\tilde{\Omega}^h$ ($h \in [1,N]$). As illustrated in Fig. 1, each control volume $\bar{\Omega}_k$ contains exactly one node $\boldsymbol{x}_k$ of the dual coarse grid in its interior. These two grids can be much coarser than the underlying fine grid, on which the mobility field is represented. The reduction of degrees of freedom to describe the fine pressure p_f is achieved through the approximation

$$p_f(\boldsymbol{x}) \approx p'(\boldsymbol{x}) = \sum_{h=1}^{N}\left[\sum_{k=1}^{M}\Phi_k^h(\boldsymbol{x})\bar{p}_k + \Phi^h(\boldsymbol{x})\right], \tag{11}$$

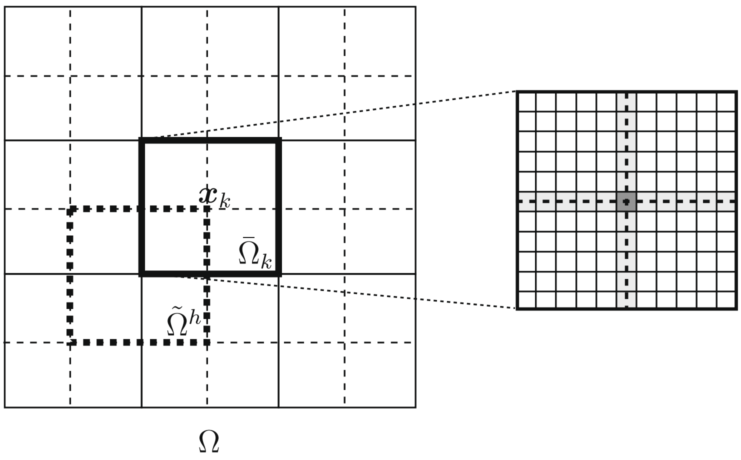

Fig. 1. The computational domain Ω with the coarse grid (solid lines) and the dual coarse grid (dashed lines); bold solid and bold dashed lines indicate a selected coarse cell $\bar{\Omega}_k$ and a selected dual coarse cell $\tilde{\Omega}^h$, respectively. Shown on the right side is an enlarged coarse cell, which contains 11×11 fine cells. The fine-scale boundary volumes of the adjacent dual coarse cells are depicted in grey.

where $\bar{p}_k$ are the pressure values at the nodes $\boldsymbol{x}_k$. Opposed to the classical finite-element methods, basis functions Φ_k^h and correction functions Φ^h are not analytical functions, but local numerical solutions of problem (10) on $\tilde{\Omega}^h$ without and with right-hand side, respectively; subject to the reduced problem boundary conditions

$$(\tilde{\boldsymbol{n}}^h \cdot \nabla)\Big((\boldsymbol{\lambda}_t \cdot \nabla \Phi_k^h) \cdot \tilde{\boldsymbol{n}}^h\Big) = 0 \tag{12}$$

and

$$(\tilde{\boldsymbol{n}}^h \cdot \nabla)\Big((\boldsymbol{\lambda}_t \cdot \nabla \Phi^h) \cdot \tilde{\boldsymbol{n}}^h\Big) = r^h \tag{13}$$

at $\partial\tilde{\Omega}^h$ with $\tilde{\boldsymbol{n}}^h$ being the unit normal vector pointing out of $\tilde{\Omega}^h$. At the dual-grid nodes $\boldsymbol{x}_l$, $\Phi_k^h(\boldsymbol{x}_l) = \delta_{kl}$ and $\Phi^h(\boldsymbol{x}_l) = 0$. By construction, Φ_k^h and Φ^h are set to zero outside of $\tilde{\Omega}^h$. An illustration of 2D basis and correction functions is shown in Fig. 2.

To derive a linear system for the coarse pressure values $\bar{p}_k$, we substitute p in Eq. (10) with the approximate expression (11) and integrate over $\bar{\Omega}_l$, which leads to

$$-\int_{\bar{\Omega}_l} \nabla \cdot (\boldsymbol{\lambda}_t \cdot \nabla p') d\Omega = -\int_{\bar{\Omega}_l} \nabla \cdot \left(\boldsymbol{\lambda}_t \cdot \nabla \left(\sum_{h=1}^{N} \left(\sum_{k=1}^{M} \Phi_k^h \bar{p}_k + \Phi^h\right)\right)\right) d\Omega = \int_{\bar{\Omega}_l} q \, d\Omega \tag{14}$$

for all $l \in [1, M]$. With the Gauss theorem one obtains

$$-\int_{\partial\bar{\Omega}_l} \left(\boldsymbol{\lambda}_t \cdot \sum_{h=1}^{N} \left(\sum_{k=1}^{M} \bar{p}_k \nabla \Phi_k^h + \nabla \Phi^h\right)\right) \cdot \bar{\boldsymbol{n}}_l \, d\Gamma = \sum_{k=1}^{M} \bar{p}_k \sum_{h=1}^{N} \int_{\partial\bar{\Omega}_l} (-\boldsymbol{\lambda}_t \cdot \nabla \Phi_k^h) \cdot \bar{\boldsymbol{n}}_l \, d\Gamma + \sum_{h=1}^{N} \int_{\partial\bar{\Omega}_l} (-\boldsymbol{\lambda}_t \cdot \nabla \Phi^h) \cdot \bar{\boldsymbol{n}}_l \, d\Gamma = \int_{\bar{\Omega}_l} q \, d\Omega, \tag{15}$$

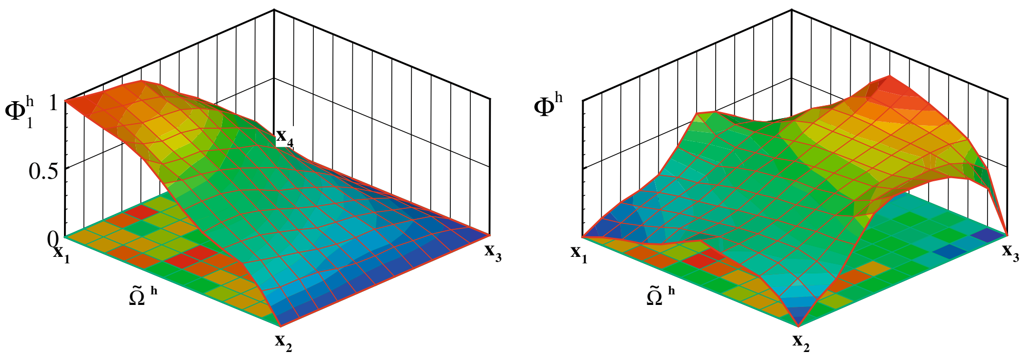

Fig. 2. Illustration of the basis function Φ_1^h (left) and the correction function Φ^h (right) for elliptic problems. The permeability map for the corresponding localized domain $\tilde{\Omega}^h$ is partly shown on the base surfaces.

which results in the linear system

$$A_{lk}\bar{p}_k = b_l \tag{16}$$

for $\bar{p}_k$ with

$$A_{lk} = \sum_{h=1}^{N} \int_{\partial\bar{\Omega}_l} (-\boldsymbol{\lambda}_t \cdot \nabla\Phi_k^h) \cdot \bar{\boldsymbol{n}}_l \, d\Gamma \tag{17}$$

and

$$b_l = \int_{\bar{\Omega}_l} q \, d\Omega - \sum_{h=1}^{N} \int_{\partial\bar{\Omega}_l} (-\boldsymbol{\lambda}_t \cdot \nabla\Phi^h) \cdot \bar{\boldsymbol{n}}_l \, d\Gamma. \tag{18}$$

The unit normal vector $\bar{\boldsymbol{n}}_l$ points out of $\bar{\Omega}_l$. Note that the right-hand side b_l also contains the effects of the fine-scale fluxes across $\partial\bar{\Omega}_l$ induced by the correction functions Φ^h.

With $\bar{p}_k$ and the superposition (11) one obtains the fine-scale pressure p', which is an approximation of the fine-scale reference solution p_f. An interesting property of this MSFV method is that the difference between p' and p_f is solely due to the localization assumption (13), i.e. with

$$r^h = (\tilde{\boldsymbol{n}}^h \cdot \nabla)\big((\boldsymbol{\lambda}_t \cdot \nabla p_f) \cdot \tilde{\boldsymbol{n}}^h\big) \quad \text{at } \partial\tilde{\Omega}^h \ \forall h \in [1, N] \tag{19}$$

the two fine-scale pressure fields become identical.

It has been shown for a wide range of challenging test cases that the MSFV method with reduced problem boundary conditions ($r^h = 0$) leads to very accurate results.

For multiphase problems, a conservative fine-scale velocity field is required to honor mass balance of the transported phase saturations. While the velocity

$$\boldsymbol{u}' = -\boldsymbol{\lambda}_t \cdot \nabla p' \tag{20}$$

fulfills this requirement in a weak sense, i.e. for each coarse volume $\bar{\Omega}_k$, the fine-scale velocity field $\boldsymbol{u}'$ is non-conservative at the dual-cell boundaries. Therefore, if one is interested in solving saturation transport on the fine grid, a further step is required. To reconstruct a conservative fine-scale velocity field $\boldsymbol{u}''$, which is consistent with $\boldsymbol{u}'$, the additional local problems

$$-\nabla \cdot (\boldsymbol{\lambda}_t \cdot \nabla p_k'') = q \quad \text{on } \bar{\Omega}_k \tag{21}$$

with

$$(\boldsymbol{\lambda}_t \cdot \nabla p_k'') \cdot \bar{\boldsymbol{n}}_k = (\boldsymbol{\lambda}_t \cdot \nabla p') \cdot \bar{\boldsymbol{n}}_k \quad \text{at } \partial\bar{\Omega}_k \tag{22}$$

are solved. Note that the velocity field

$$\boldsymbol{u}'' = \begin{cases} -\boldsymbol{\lambda}_t \cdot \nabla p_k'' & \text{on } \bar{\Omega}_k, \\ -\boldsymbol{\lambda}_t \cdot \nabla p' & \text{at } \partial\bar{\Omega}_k \end{cases} \tag{23}$$

for all $k \in [1, M]$ is conservative (provided p'' is obtained with a conservative scheme) and can be employed to solve transport equations on the fine grid [7].

An important property of the MSFV method is its adaptivity. For example, the conservative velocity reconstruction described above is only required in those coarse cells $\bar{\Omega}_k$, where fine-scale transport is of interest. Moreover, it is very important that the basis and correction functions can be stored and reused for subsequent time steps. They have to be recomputed only in those dual cells $\tilde{\Omega}^h$, where changes of the coefficient $\boldsymbol{\lambda}_t$ or (for the correction functions) the right-hand side q exceed a specified limit [14,16,15]. Next, we explain our new MSFV method for compressible multiphase flow, i.e. for parabolic problems.

4. MSFV method for compressible multiphase flow (parabolic)

For incompressible flow, as explained in the previous section, basis and correction functions are local numerical solutions of an elliptic problem with and without right-hand side, respectively. Here, this idea is consistently generalized for compressible multiphase flow. Therefore, the basis and correction functions are computed by solving the localized problems

$$\frac{C}{\Delta t}\Phi_k^h - \nabla \cdot (\boldsymbol{\lambda}_t \cdot \nabla\Phi_k^h) = 0 \tag{24}$$

and

$$\frac{C}{\Delta t}\Phi^{h^\nu} - \nabla \cdot (\boldsymbol{\lambda}_t \cdot \nabla\Phi^{h^\nu}) = RHS^\nu + \frac{C}{\Delta t}p'^\nu \tag{25}$$

on the dual coarse cells $\tilde{\Omega}^h$; again subject to the reduced problem boundary condition as in the previously explained elliptic case (Eqs. (12) and (13)). In contrary to the previous works [25,26], there is no iteration superscript for the basis function calculations, i.e. they have to be computed only once while the correction functions are computed iteratively and take care of all pressure dependencies. Note that in 3D there exist 8 times more basis than correction functions. When convergence occurs, the first term on the left-hand side of Eq. (8) cancels out. Hence, the specific value of C does not affect the numerical value of the converged solution, but affects the convergence rate. As C is a monotone function of the pressure, it can be computed based on either p'^{ν} or p'^{n} (or some reference pressure). In this work, to keep the basis functions totally out of the iteration loop, C is computed based on p'^{n}. An illustration of the basis and correction functions for parabolic problems (Eqs. (24) and (25)) is given in Fig. 3. Moreover, Fig. 3(left) emphasizes the difference between a basis function, which is calculated based on the full parabolic equation, i.e. Eq. (8), and the elliptic part of it, i.e. without the $\frac{C}{\Delta t}\Phi_k^h$ term (wireframe). Finally, the time size for calculation of basis and correction functions are the same as that of the global parabolic problem.

To derive a linear system for the coarse pressure values $\bar{p}_k$, we follow exactly the described procedure for incompressible flow. Since the basis and correction functions are solutions of the full parabolic problem in the localized domains, no further consideration in the coarse scale system, such as averaging the accumulation term, is necessary (opposed to [26]). Substituting expression (11) into Eq. (8) and integrating over $\bar{\Omega}_l$ leads to

$$\int_{\bar{\Omega}_l} \frac{C}{\Delta t}\left(\sum_{h=1}^{N}\left(\sum_{k=1}^{M}\bar{p}_k^{\nu+1}\Phi_k^h + \Phi^{h^\nu}\right) - p'^{\nu}\right)d\Omega - \int_{\partial\bar{\Omega}_l}\left(\boldsymbol{\lambda}_t\cdot\sum_{h=1}^{N}\left(\sum_{k=1}^{M}\bar{p}_k^{\nu+1}\nabla\Phi_k^h + \nabla\Phi^{h^\nu}\right)\right)\cdot\bar{\boldsymbol{n}}_l\,d\Gamma$$
$$= \int_{\bar{\Omega}_l} RHS^{\nu}\,d\Omega + \int_{\bar{\Omega}_l} q\,d\Omega, \tag{26}$$

which results in an iterative linear system

$$A_{lk}\bar{p}_k^{\nu+1} = b_l^{\nu} \tag{27}$$

for $\bar{p}_k^{n+1}$ with

$$A_{lk} = \sum_{h=1}^{N}\left(\int_{\bar{\Omega}_l}\frac{C}{\Delta t}\Phi_k^h\,d\Omega - \int_{\partial\bar{\Omega}_l}(\boldsymbol{\lambda}_t\cdot\nabla\Phi_k^h)\cdot\bar{\boldsymbol{n}}_l\,d\Gamma\right) \tag{28}$$

and

$$b_l^{\nu} = \int_{\bar{\Omega}_l}\left(RHS^{\nu} + \frac{C}{\Delta t}p'^{\nu}\right)d\Omega - \sum_{h=1}^{N}\left(\int_{\bar{\Omega}_l}\frac{C}{\Delta t}\Phi^{h^\nu}d\Omega - \int_{\partial\bar{\Omega}_l}(\boldsymbol{\lambda}_t\cdot\nabla\Phi^{h^\nu})\cdot\bar{\boldsymbol{n}}_l\,d\Gamma\right). \tag{29}$$

Using $\bar{p}^{\nu+1}$ for $\bar{p}$ in expression (11) gives the new fine-scale pressure field $p'^{\nu+1}$. The iterative procedure is repeated until p' converges, i.e. until $\|p'^{\nu+1} - p'^{\nu}\|_\infty < \epsilon$, where ϵ is a specified convergence parameter. As already mentioned, a conservative velocity field must be reconstructed in order to solve the saturation transport equations on the fine grid. We reconstruct it by solving Eq. (8) locally subject to the Neumann boundary conditions based on p'^{n+1}; similar as in the incompressible case. The resulting pressure field p''^{n+1} is considered as the final solution at the time step $n+1$. Finally, this conservative total velocity field is employed to explicitly solve the saturation Eq. (3) using a second order upwind scheme.

From the parabolic basis function calculation (Eq. (24)) and the coarse-scale matrix A (Eq. (28)) it is clear that the accumulation term (compressibility coefficient) appears as a stencil in the coarse-scale system, and not only as a diagonal contribution. This is an important factor for the high accuracy of the method, which will be illustrated for several test cases

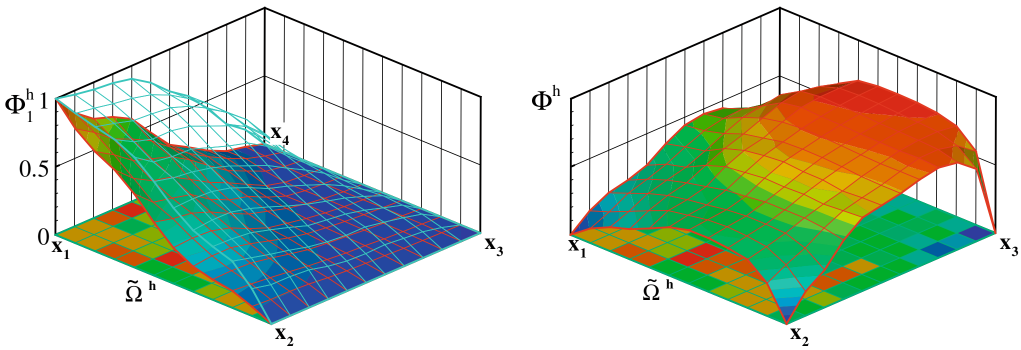

Fig. 3. Illustration of the basis function Φ_1^h (left) and correction function Φ^h (right) for parabolic problems. The permeability map for the corresponding localized domain $\tilde{\Omega}^h$ is partly shown on the base surfaces. Also shown (left) is the wire-frame of the basis function for the corresponding elliptic problem, i.e. without first term on the left-hand side of Eq. (24).

Table 1
Algorithmic outline of one time step with the MSFV method for compressible multiphase flow.

initialize $\mathbf{p}'^{(t=n)}$
$\forall h$: $\forall k$: compute basis functions $\mathbf{\Phi}_k^h$; Eq. (24)
from $\nu = 1$ to convergence {
$\forall h$: compute correction functions $\mathbf{\Phi}^{h^\nu}$; Eq. (25)
solve coarse system $\boldsymbol{A} \cdot \bar{\boldsymbol{p}}^{\nu+1} = \boldsymbol{b}^\nu$; Eq. (27)
reconstruct $\boldsymbol{p}'^{\nu+1}$; Eq. (11)
update properties
$\nu \leftarrow \nu + 1$
}
reconstruct p''^{n+1} and calculate conservative velocity field; Eq. (8)
solve saturation transport equations; Eq. (3)

in the next section. An algorithmic overview of the proposed MSFV method for compressible multiphase flow problems is presented in Table 1.

5. Numerical results

5.1. Single-phase flow

To analyze the performance of the new scheme compared to the previous studies, first a one-dimensional (1D) homogeneous single-phase flow problem is studied. No gravity effects are considered and the domain is initially filled with ideal gas at atmospheric pressure (14.7 psi). The right boundary is kept at a constant pressure of 14.7 psi and at time $t = 0$, the pressure at the left boundary is increased to 10 atm (147.0 psi). We recall the state equation of ideal gas under isothermal conditions, i.e.

$$\frac{\rho_g}{\rho_{g0}} = \frac{p}{p_0}, \tag{30}$$

where ρ_{g0} is the density at atmospheric pressure p_0. The computational domain contains 105 fine cells and 5 coarse cells. Fig. 4 shows results at different non-dimensional times $t^* = t/\tau$, where

$$\tau = \frac{\mu \phi L^2}{\bar{k}(p_l - p_r)}. \tag{31}$$

In Eq. (31), $\bar{k}$ is the average permeability in the domain, L is the length of the domain, and $(p_l - p_r)$ is the pressure difference between the left and right boundaries. It can be observed that the new MSFV method (Fig. 4(left)) leads to results, which are

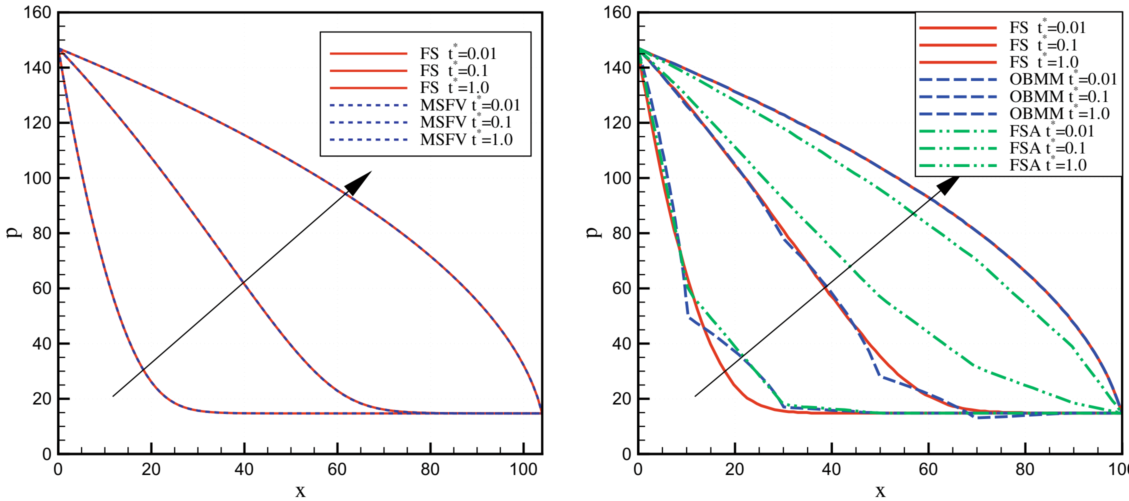

Fig. 4. 1D single-phase gas injection test case: pressure at three different times. Shown are the new MSFV and fine-scale reference solutions (left) using 105 fine and 5 coarse cells together with previous multiscale solutions presented in [25] (right) using 100 fine and 5 coarse cells. FSA based multiscale method was developed by Lunati and Jenny [24] and OBMM method was developed by Zhou and Tchelepi [25].

virtually identical to the fine-scale reference solutions. It is remarkable that unlike in previous works [24,25] (Fig. 4(right)) no peculiarities in the results were observed for the early transient phase.

Since no localization assumption is required for 1D problems, the MSFV and fine-scale solutions are identical up to machine accuracy. Note that in 2D or 3D, convergence of the MSFV solution can be achieved (even for highly anisotropic heterogeneous problems) by iteratively improving the localization assumption, i.e. by improving the boundary condition of the local problems [22].

5.2. Depletion in 1D and 2D

As a second test case, depletion of a liquid–gas reservoir is studied. No gravity effects are considered and the reservoir pressure is initially at 10 atmosphere (147.0 psi). At $t = 0$ the pressure at the right boundary is decreased to one atmosphere (14.7 psi), while it is kept constant at the left boundary. At top and bottom, no-flow boundary conditions are applied. The domain is initially filled with 50% ideal gas and 50% water. Porosity of the medium and viscosity ratio μ_g/μ_w are set to 0.1 and 1.8×10^{-2} everywhere, and the water compressibility is neglected. Water saturation S_w at the left boundary is kept constant at *0.5*. For all test cases presented in this paper, relative permeability is modeled as a quadratic function of the corresponding phase saturation.

First, a homogeneous 1D domain containing 105 fine and 5 coarse cells is considered. Fig. 5 shows the MSFV results (pressure and saturation) at different times and it can be observed that they are in perfect agreement with the fine-scale reference solutions. Another study was considered with a 2D permeability field, which was extracted from the top layer of the SPE comparative test case 10 [28] (Fig. 6). The grid consists of 220×55 fine and 20×5 coarse cells. MSFV pressure and saturation maps at $t^* = 10^{-4}$, $t^* = 10^{-3}$, and $t^* = 10^{-2}$ are depicted on the right of Figs. 7 and 8, respectively, and the corresponding fine-scale reference solutions are shown on the left. For better comparison, the saturation maps are only shown for $x \geqslant 160$. In addition, Figs. 9 and 10 show results at $t^* = 10^{-1}$ and $t^* = 1$, respectively. Again, the MSFV and fine-scale solutions are in excellent agreement.

5.3. Five-spot problem: ideal gas injection

As another test case, the injection of an ideal gas into a 2D heterogeneous domain with the same permeability as shown in Fig. 6 is studied. No-flow boundary conditions are applied everywhere. The domain is initially filled with oil at atmospheric

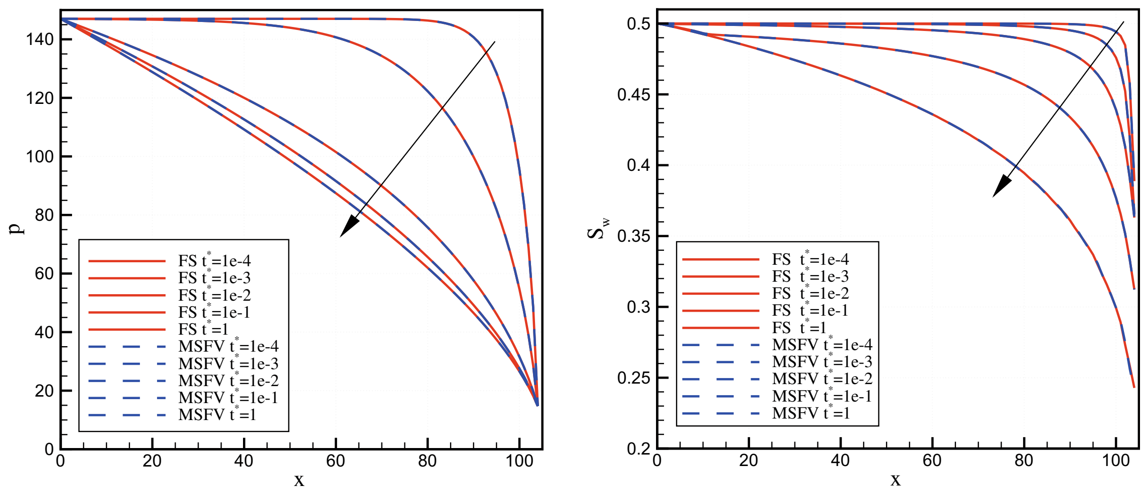

Fig. 5. Depletion of a homogeneous 1D domain: fine-scale solutions (using 105 cells) compared with the MSFV results (using 5 coarse cells); pressure (left) and water saturation (right) at different non-dimensional times.

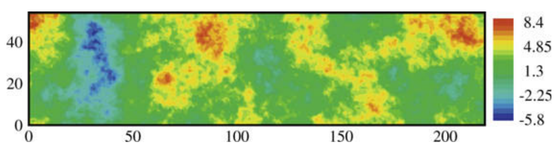

Fig. 6. Natural logarithm of the permeability extracted from the top layer of the three-dimensional SPE10 test case [28]; for a 220×55 fine grid.

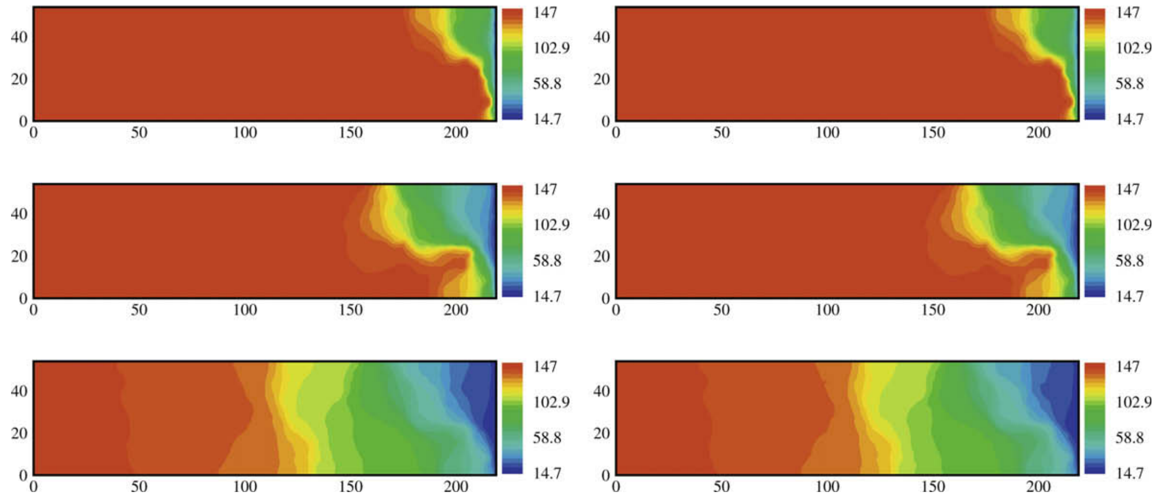

Fig. 7. Heterogeneous 2D depletion test case: pressure filed obtained from the fine-scale simulation using 220 × 55 fine cells (left) and from the MSFV simulation using 20 × 5 coarse cells (right) at $t^* = 10^{-4}$ (top), $t^* = 10^{-3}$ (middle), and $t^* = 10^{-2}$ (bottom).

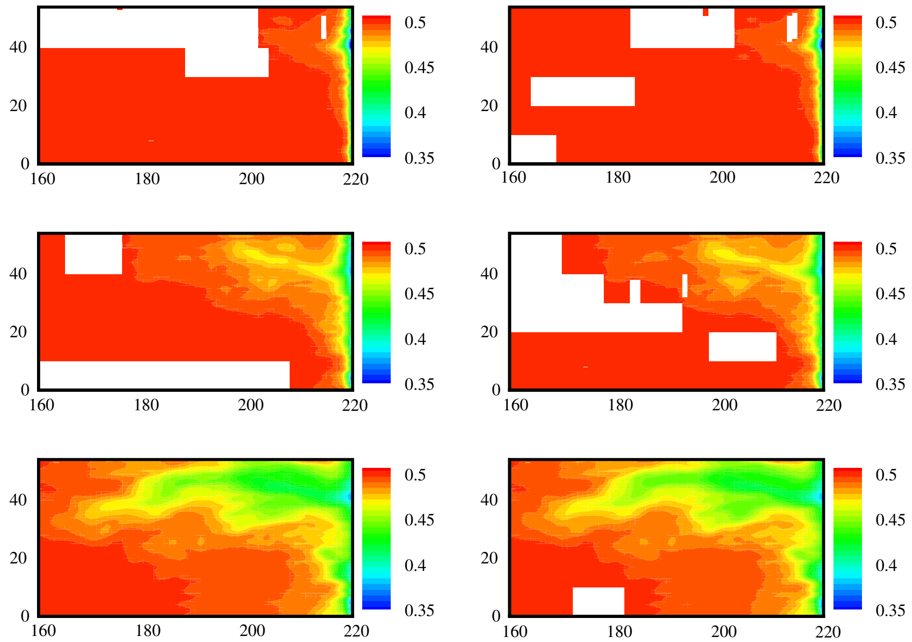

Fig. 8. Heterogeneous 2D depletion test case: water saturation maps obtained from the fine-scale simulation using 220 × 55 fine cells (left) and for the MSFV simulation using 20 × 5 coarse cells (right) at $t^* = 10^{-4}$ (top), $t^* = 10^{-3}$ (middle), and $t^* = 10^{-2}$ (bottom). The results are only depicted for $x \geqslant 160$.

pressure (14.7 psi) and no gravity effects are taken into account. At $t \geqslant 0$, an ideal gas is injected at a constant volumetric rate from the left-bottom corner (fine cell (1,1)) and production occurs at the upper-right corner (fine cell (220,55)) at a constant pressure of 14.7 psi. The viscosity ratio is 10 and it is assumed that the oil density obeys the isothermal linear equation of state, i.e. that

$$\frac{\rho_o}{\rho_{o0}} = 1 + 10^{-3}(p - p_0), \tag{32}$$

where ρ_{o0} is the density at the reference pressure $p_0 = 14.7$ psi. Results are shown in Fig. 11 after 0.132 PVI (Pore Volume Injected). For better comparison, Fig. 12 shows the absolute pressure and saturation differences between the fine-scale and MSFV solutions. Again, a very good agreement can be observed.

bottom left corner (fine cell (1,1)), while production occurs from the top right of the domain (fine cell (44,44)) at a constant pressure of 147.0 psi. The density ratio at STC (Stock Tank Condition) ρ_{0o}/ρ_{0g} is 100, the viscosity ratio μ_o/μ_g is 5, and the porosity is 0.2. The grid contains 44×44 fine cells and 4×4 coarse cells with no-flow boundary condition everywhere (Fig. 16). Fine-scale and MSFV pressure and saturation solutions are presented in Fig. 17 after 0.08 PVI.

For better comparison, Fig. 18 depicts the absolute differences between the fine-scale and MSFV results. It can be observed that there is very good agreement.

5.5. Limitations of the MSFV method

As shown in the previous subsections, the MSFV method provides highly accurate results for many challenging test cases. This is not always the case, however, which is demonstrated for the following problematic test cases. The first of these test cases, employs the permeability distribution shown in Fig. 13 (from SPE10 bottom layer). The grids, initial, and boundary conditions correspond to the previously shown quarter-five-spot test case, but here only single-phase gas flow is considered. Gas is injected at the upper-left corner at a constant rate and production occurs at the bottom-right corner. A time step size of $\Delta t = 2.657 \times 10^{-3}$ PVI is chosen and Fig. 19 shows fine-scale and MSFV pressure solutions after one time step. One can observe local pressure peaks in both the non-conservative and conservative MSFV pressure fields (p' and p'', respectively), which are unphysical. Moreover, the size of these peaks grows with time.

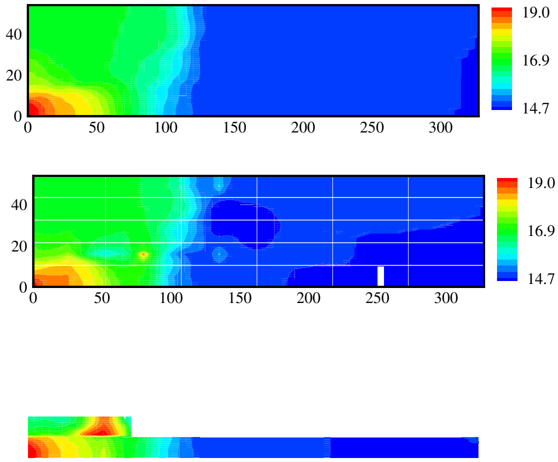

iterations, in which the boundary conditions of the local problems leading to the correction functions are updated based on the most actual fine-scale pressure reconstruction. This iterative MSFV (i-MSFV) method is convergent, i.e. exact reference solutions can be achieved without initially solving a global fine-scale problem to improve the local boundary conditions [11,9,29,32]. Another approach, which employes a reconstructed global solution to improve the localization assumptions, is the adaptive local–global (ALG) upscaling approach [33–35]. The proposed ALG method leads to improved solutions for both the upscaling [33] and the multiscale finite volume element (MSFVE) [35] methods. However, neither the ALG-upscaling approach nor the ALG-MSFVE method converge to the reference fine-scale solutions up to the machine accuracy.

As mentioned above, the recently proposed iterative MSFV (i-MSFV) method [22] improves the boundary conditions of the localized problems iteratively and the solutions converge to the fine-scale reference. It can either be used as a multiscale method (no iteration) or as an efficient iterative linear solver (with enough iterations). In each iteration, the boundary conditions of the localized problems leading to the correction functions are updated based on a pressure field, which results from smoothing $p_s'^{\nu}$, i.e. the reconstruction after the previous iteration. In other words, the localization condition (19) is replaced by the iterative expression

$$r^{h^{\nu}} = (\tilde{\boldsymbol{n}}^h \cdot \nabla)\big((\boldsymbol{\lambda} \cdot \nabla p_s'^{\nu}) \cdot \tilde{\boldsymbol{n}}^h\big) \quad \text{at } \partial\tilde{\Omega}^h \ \forall h \in [1, N]. \tag{33}$$

Since in the new MSFV method for parabolic problems the correction functions are recomputed anyhow after each iteration step due to the pressure dependent parameters, little additional cost is involved to iteratively update the localization boundary conditions at the same time as described above. Note that no further modifications are necessary to apply the i-MSFV method for compressible problems.

The smoother is essential for convergence and one can think of many variants. Here, line-relaxation (LR) is used, since it proved to be very effective for cases with highly anisotropic permeability fields or stretched grids [22]. LR is applied n_s times (inner loop) in all spacial directions. A pseudo code of the overall algorithm is presented in Table 2. Note that besides the localization boundary conditions, also the coefficients are updated based on the latest smoothed pressure field $\mathbf{p}_s'^{\nu+1}$. If the outer loop is repeated until convergence is achieved, i.e. until $\|p'^{\nu+1} - p'^{\nu}\|_\infty \leqslant \epsilon$, then there is no need to reconstruct the conservative pressure field p''^{n+1}. On the other hand, if only a few iterations are performed to improve the multi-scale solution, the conservative reconstruction ensures that the reconstructed fine-scale velocity field still is conservative, even for a solution far from the converged one.

6.1. Convergence study

The performance of the i-MSFV method for compressible multiphase flow is studied for homogeneous-isotropic, heterogeneous-isotropic, homogeneous-anisotropic, and heterogeneous-anisotropic problems. All domains are initially filled with an ideal gas at atmospheric pressure (14.7 psi) and no gravity effects are considered. At $t = 0$, the pressure at the left boundary is elevated to 147.0 psi, while it is kept constant at the right boundary. No-flow boundary conditions are applied at the top and bottom walls. For the homogeneous test cases, the permeability is equal to *1* and the heterogeneous permeability fields are subdomains of the SPE10 [28] top layer ($ln(k)$ mean and variance are -0.29 and 6.66, respectively). The porosity ϕ is 0.3 for all test cases. The fine and coarse grids contain 44×44 and 4×4 coarse cells and to study the effect of anisotropy, a fine cell aspect ratio α (width over height) of 10 is employed. Fig. 21 depicts the computational domain as well as the natural logarithm (ln) of the heterogeneous permeability field.

Fig. 22 shows the pressure maps after one non-dimensional time step $\Delta t^* = \Delta t/\tau$ ($\Delta t^* = 0.03$ for the homogeneous and $\Delta t^* = 0.01$ for the heterogeneous test cases). The time scale τ is computed based on $L_{aniso.} = \alpha L_{iso.}, \bar{k}_{hom.} = 1$, and $\bar{k}_{het.} = 11.2421$.

Fig. 23 shows the base-10 logarithm (log) of the maximum pressure error in the domain normalized with the pressure difference between the left and right boundaries, i.e. $\log(\epsilon)$ with $\epsilon = \|p'^{\nu+1} - p_f^{n+1}\|_\infty/(p_l - p_r)$, as a function of i-MSFV iterations and smoothing steps (per iteration) n_s for the homogeneous (Fig. 23a and c) and heterogeneous (Fig. 23b and d) cases with $\alpha = 1$ (Fig. 23a and b) and $\alpha = 10$ (Fig. 23c and d).

The convergence rate of the i-MSFV method (average slope between $log(\epsilon) = -3$ and $\log(\epsilon) = -9$) as a function of Δt^* is shown in Fig. 24 for different n_s.

Note that the i-MSFV algorithm (Table 2) and the MSFV algorithm (Table 1) for compressible multiphase flow are iterative schemes converging to the original non-linear pressure equation (Eq. (4)) exactly and approximately, respectively. It is clear from Fig. 25 that the i-MSFV method converges to the fine-scale reference solutions faster than the MSFV method to approximate solutions. In other words, improvement of the localization condition not only improves the quality of the results, but also enhances the convergence rate. The only additional cost for the i-MSFV method compared with the MSFV method is due to the smoothing step.

6.2. Multiphase flow problems

As described in the previous subsection, one may not be interested to use the i-MSFV method as a linear solver, but as an algorithm to improve the quality of the MSFV results. Therefore, in this subsection we consider the previously described quarter-five-spot test case with the permeability of SPE10 top layer (Fig. 6) and $\alpha = 10$. Remember that for this test case the MSFV method leads to unphysical solutions. Phase properties, initial and boundary conditions are the same as for the previously described test case. Gas is injected with a constant rate at the upper-right corner (fine cell (220,55)) and oil is

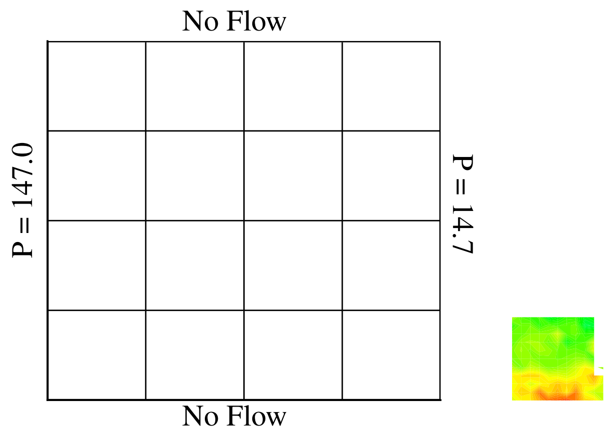

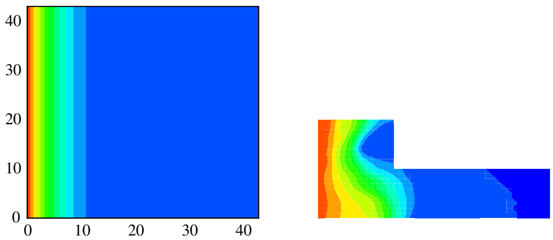

produced from the bottom-left corner (fine cell $(1,1)$), where the pressure is kept constant at 14.7 psi (initial pressure). Here, only two i-MSFV iterations ($n_v = 2$) are performed in each time step with $n_s = 10$. The conservative pressure field p'' is

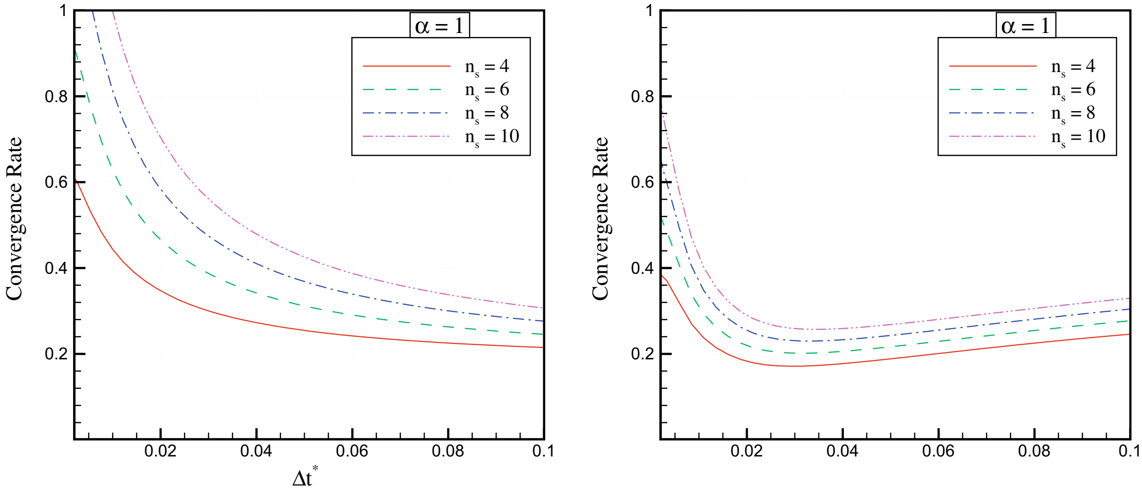

$\alpha = 1$
$n_s = 4$
$n_s = 6$
$n_s = 8$
$n_s = 10$
Convergence Rate
0.2
0.4
0.6
0.8
1
0.02
0.04
0.06
0.08
0.1
Δt^*
$\alpha = 1$
$n_s = 4$
$n_s = 6$
$n_s = 8$
$n_s = 10$
Convergence Rate
0.2
0.4
0.6
0.8
1
0.02
0.04
0.06
0.08
0.1

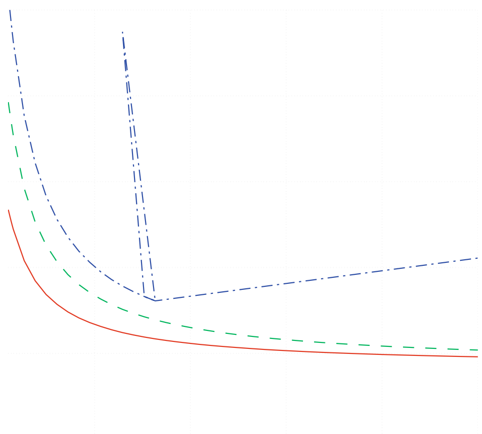

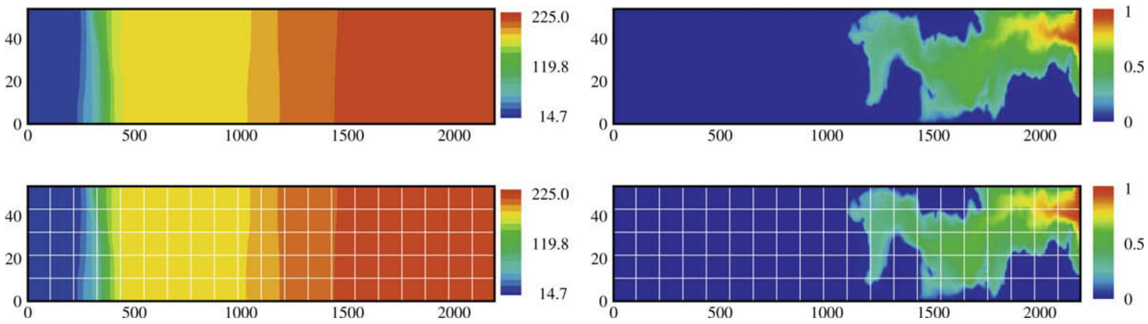

Fig. 26. i-MSFV method for multiphase flow with $\alpha = 10$ and the permeability field of Fig. 6: pressure field (left) and gas saturation maps (right) obtained for the fine-scale simulation using 220×55 fine cells (top) and from the i-MSFV simulation using 20×5 coarse cells (bottom) at $t = 0.2116$ PVI. For the i-MSFV simulation, two iterations with $n_s = 10$ per time was employed.

computed once at the end of each time step. Fig. 26 shows the results after 0.2116 PVI. It is clear that results are virtually identical. One could also employ the idea of infrequently updating the boundary conditions [22] to improve the computational efficiency, but this is beyond the scope of this paper.

7. Conclusions

A new multiscale finite-volume method for parabolic problems arising from compressible multiphase flow in porous media is presented. In this scheme, the basis and correction functions are calculated based on the full parabolic governing equation, and not just based on the elliptic part of it. At the same time, the coefficients appearing in the basis function equations are kept pressure independent. This is crucial for high computational efficiency, since it allows to keep the basis functions for multiple iterations and time steps. During the iterative procedure, only the correction functions have to be updated (in 3D, there exist 8 times more basis functions than correction functions). It is shown for highly compressible scenarios that the new scheme leads to results, which are in very good agreement with the fine-scale reference solutions. In particular, during transient times the new method outperforms existing multiscale methods for compressible multiphase cases. The reason for the high accuracy of the proposed MSFV method is due to the minimum assumptions that have been applied to develop the method, i.e. considering full governing equation for calculation of basis and correction functions. The only assumption applied to this framework is the localization condition, which is trivial and inevitable for the multiscale methods. Therefore, for 1D problems, where there is no localization assumption, results of the proposed MSFV method and the reference fine-scale solutions are identical.

Moreover, an i-MSFV method for parabolic problems was described. It ensures that the multiscale solutions converge to the fine-scale reference. Numerical convergence of the method was demonstrated for many test cases for different numbers of smoothing steps n_s and different non-dimensional time step sizes Δt^*. It was shown that the i-MSFV method (converging to fine-scale reference solutions) is more efficient than the MSFV method (converging to approximate solutions). The only additional cost is due to the smoothing step, which is minimal and can be reduced by updating the boundary conditions only infrequently, i.e. not every time steps.

Acknowledgment

This work was partly supported by Chevron/Schlumberger Intersect Alliance Technology.

References

[1] T.Y. Hou, X.-H. Wu, A multiscale finite element method for elliptic problems in composite materials and porous media, J. Comput. Phys. 134 (1997) 169–189.
[2] T. Hughes, G. Feijoo, L. Mazzei, J. Quincy, The variational multiscale method – a paradigm for computational mechanics, Comput. Methods Appl. Mech. Eng. 166 (1998) 3–24.
[3] T.Y. Hou, X.-H. Wu, Z. Cai, Convergence of a multiscale finite element method for elliptic problems with rapidly oscillating coefficients, Math. Comput. 68 (227) (1999) 913–993.
[4] Y. Efendiev, V. Ginting, T. Hou, R. Ewing, Convergence of a nonconforming multiscale finite element method, SIAM J. Numer. Anal. 37 (3) (2000) 888–910.
[5] T. Arbogast, Numerical subgrid upscaling of two-phase flow in porous media, in: Lect. Notes Phys., Numerical Treatment of Multiphase Flows in Porous Media 552 (3–4) (2000) 35–49.
[6] Z. Chen, T.Y. Hou, A mixed multiscale finite element method for elliptic problems with oscillating coefficients, Math. Comput. 72 (242) (2002) 541–576.
[7] P. Jenny, S.H. Lee, H.A. Tchelepi, Multi-scale finite-volume method for elliptic problems in subsurface flow simulation, J. Comput. Phys. 187 (2003) 47–67.
[8] Y. Efendiev, T. Hou, V. Ginting, Multiscale finite element methods for nonlinear problems and their applications, Commun. Math. Sci. 2 (4) (2004) 553–589.

[9] J.E. Aarnes, On the use of a mixed multiscale finite element method for greater flexibility and increased speed or improved accuracy in reservoir simulation, Multiscale Model. Simul. 2 (3) (2004) 421–439.
[10] V. Ginting, Analysis of two-scale finite volume element method for elliptic problem, J. Numer. Math. 12 (2004) 119–141.
[11] J.E. Aarnes, V. Kippe, K.-A. Lie, Mixed multiscale finite elements and streamline methods for reservoir simulation of large geomodels, Adv. Water Resour. 28 (3) (2005) 257–271.
[12] R. Juanes, F.X. Dub, A locally conservative variational multiscale method for the simulation of porous media flow with multiscale source terms, Comput. Geosci. 12 (2008) 273–295.
[13] T. Arbogast, Implementation of a locally conservative numerical subgrid upscaling scheme for two-phase darcy flow, Comput. Geosci. 6 (3-4) (2002) 453–481.
[14] P. Jenny, S.H. Lee, H.A. Tchelepi, Adaptive multiscale finite volume method for multi-phase flow and transport, SIAM Multiscale Model. Simul. 3 (1) (2004) 50–64.
[15] H.A. Tchelepi, P. Jenny, S.H. Lee, C. Wolfsteiner, Adaptive multiscale finite-volume framework for reservoir simulation, SPE J. 12 (2) (2007) 188–195. SPE-93395-PA.
[16] P. Jenny, S.H. Lee, H.A. Tchelepi, Adaptive fully implicit multi-scale finite-volume method for multi-phase flow and transport in heterogeneous porous media, J. Comput. Phys. 217 (2006) 627–641.
[17] I. Lunati, P. Jenny, A multiscale finite-volume method for three-phase flow influenced by gravity, in: Proceedings of XVI International Conference on Computational Methods in Water Resources (CMWR XVI), Copenhagen, Denmark, 2006, pp. 1–8.
[18] I. Lunati, P. Jenny, Multiscale finite-volume method for density-driven flow in porous media, Comput. Geosci. 12 (3) (2008) 337–350.
[19] C. Wolfsteiner, S.H. Lee, H.A. Tchelepi, Well modeling in the multiscale finite volume method for subsurface flow simulation, SIAM Multiscale Model. Simul. 5 (3) (2006) 900–917.
[20] P. Jenny, I. Lunati, Well modeling in the multi-scale finite volume context, Proc. Appl. Math. Mech. (PAMM) 7 (2007) 1024601–1024602.
[21] P. Jenny, I. Lunati, Modeling complex wells with the multi-scale finite volume method, J. Comput. Phys. 228 (3) (2009) 687–702.
[22] H. Hajibeygi, G. Bonfigli, M.A. Hesse, P. Jenny, Iterative multiscale finite-volume method, J. Comput. Phys. 227 (2008) 8604–8621.
[23] G. Bonfigli, P. Jenny, An efficient multi-scale poisson solver for the incompressible Navier–Stokes equations with immersed boundaries, J. Comput. Phys. 228 (12) (2009) 4568–4587.
[24] I. Lunati, P. Jenny, Multiscale finite-volume method for compressible multiphase flow in porous media, J. Comput. Phys. 216 (2) (2006) 616–636.
[25] H. Zhou, H.A. Tchelepi, Operator based multiscale method for compressible flow, SPE J. 13 (2) (2008) 267–273. SPE-106254-PA.
[26] S.H. Lee, C. Wolfsteiner, H.A. Tchelepi, Multiscale finite-volume formulation for multiphase flow in porous media: black oil formulation of compressible, three-phase flow with gravity, Comput. Geosci. 12 (3) (2008) 351–366.
[27] K. Aziz, A. Settari, Petroleum Reservoir Simulation, Blitzprint Ltd., Cagary, Alberta, 2002.
[28] M.A. Christie, M.J. Blunt, Tenth spe comparative solution project: A comparison of upscaling techniques. SPE 66599, presented at the SPE Symposium on Reservoir Simulation, Houston, February, 2001, pp. 1–13.
[29] V. Kippe, J.E. Aarnes, K.-A. Lie, A comparison of multiscale methods for elliptic problems in porous media flow, Comput. Geosci. 12 (3) (2008) 377–398.
[30] P. Jenny, I. Lunati, Treating highly anisotropic subsurface flow with the multiscale finite-volume method, SIAM Multiscale Model. Simul. 6 (1) (2007) 308–318.
[31] M.A. Hesse, B.T. Mallison, H.A. Tchelepi, Compact multiscale finite volume method for heterogeneous anisotropic elliptic equations, SIAM Multiscale Model. Simul. 7 (2008) 934–962.
[32] Y. Efendiev, V. Ginting, T. Hou, R. Ewing, Accurate multiscale finite element methods for two-phase flow simulations, J. Comput. Phys. 220 (2006) 155–174.
[33] Y. Chen, L.J. Durlofsky, M. Geritsen, X.H. Wen, A coupled local–global upscaling approach for simulating flow in highly heterogeneous formations, Water Resour. Res. 26 (2003) 1041–1060.
[34] Y. Chen, L.J. Durlofsky, Efficient incorporation of global effects in upscaled models of two-phase flow and transport in heterogeneous formations, SIAM Multiscale Model. Simul. 5 (2006) 445–475.
[35] L.J. Durlofsky, Y. Efendiev, V. Ginting, An adaptive local–global multiscale finite volume element method for two-phase flow, Adv. Water Resour. 30 (2007) 576–588.